Publ. Astron. Soc. Japan (2018) 00 (0), 1–10
doi: 10.1093/pasj/psy106
Advance Access Publication Date: 2018 0

Giant cometary H II regions and molecular bow shocks in spiral arms of galaxies: M 83

Yoshiaki Sofue*

Institute of Astronomy, The University of Tokyo, 2-21-1 Osawa, Mitaka, Tokyo 181-0015, Japan

*E-mail: sofue@ioa.s.u-tokyo.ac.jp

Received 2018 July 8; Accepted 2018 August 22

Abstract

A number of giant cometary H II regions (GCHs) sheathed inside molecular bow shocks (MBSs) are found along spiral arms of the barred galaxy M 83. The open cone structure is explained by a model of an expanded H II front in a gaseous arm with a steep density gradient, and the bow shock is shown to be formed by the encounter of an H II region with the supersonic gas flow across the arm. It is suggested that dual-side compression of molecular gas at the bow head between the MBS and the GCH enhances star formation along the spiral arms.

Key words: H II regions — galaxies: spiral — galaxies: star formation — shock waves

1 Introduction

Astrophysical bow shock is a classical subject, and is observed around objects interacting with supersonic gas flows in a wide range of scales from planets to cosmic jets (Dyson 1975; van Buren et al. 1990; Ogura 1995; Wilkin 1996; Arce & Goodman 2002; Reipurth et al. 2002). Galactic-disk-scale bow structure is observed in spiral arms, where a supersonic flow in galactic rotation encounters a stagnated gaseous arm in the density-wave potential (Martos & Cox 1998; Gómez & Cox 2004a, 2004b).

On the scale of star-forming (SF) regions, a bow shock was observed at G30.5+00 $(l, b) = (30\overset{\circ}{.}5, 0^\circ)$ associated with the SF region W 43 in the tangential direction of the 4 kpc molecular arm (the Scutum arm) in thermal radio continuum emission associated with a CO line molecular arc (Sofue 1985). The molecular bow at G30.5 has recently been studied in detail based on the Nobeyama 45 m CO line survey (Sofue et al. 2018), which is called the molecular bow shock (MBS) (figure 1).

The MBS is a concave arc of molecular gas around an H II region (SF region) formed in the up-stream side of galactic rotation with respect to the SF region. An MBS is formed in such a way that the interstellar gas in the galactic supersonic flow encounters a pre-existing H II region on the down-stream side in the galactic-shock wave (figure 2).

A similar phenomenon is observed in SF regions known as a cometary H II region tailing down-stream, when a compact H II region is embedded in a flow of ambient interstellar gas (Arthur & Hoare 2006; Reid & Ho 1985; Steggles et al. 2017; van Buren et al. 1990; Fukuda & Hanawa 2000; Campbell-White et al. 2018; Deharveng et al. 2015). The current studies of cometary H II regions have been obtained for sub-parsec to parsec-scale objects inside individual SF regions. However, our observations of the association of the spiral-arm scale MBS G30.5 and the SF complex around W 43 suggests the existence of larger, spiral-arm scale cometary H II regions associated with a MBS. Namely, a MBS that develops in the up-stream side of cometary H II regions may be a common phenomenon in spiral arms.

On such a premise, we have searched for bow shock plus cometary structure in the spiral arms of nearby galaxies. In the present paper, we report on the identification of a number of bow structures in the barred spiral galaxy M 83 (NGC 5236). Assuming that dark clouds in optical images represent molecular clouds, we name them MBSs.

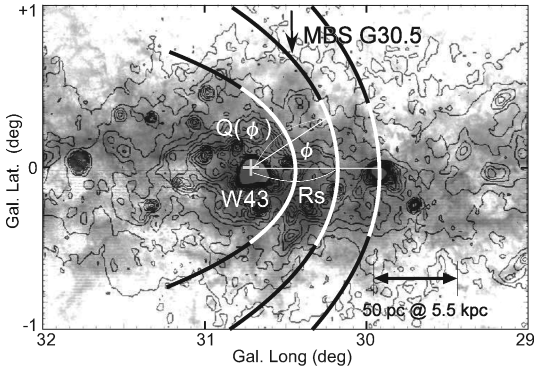

Fig. 1. ^{12}CO(J = 1–0) intensity map (gray) of the molecular bow shock (MBS) G30.5 in the Galaxy overlaid on a 10 GHz continuum map (contours) (Sofue et al. 2018), which forms a concave arc with respect to W 43. Thick lines indicate calculated bows for $R_{\mathrm{bow}} = 25$, 50, and 75 pc. The scale represents 50 pc at the distance of 5.5 kpc.

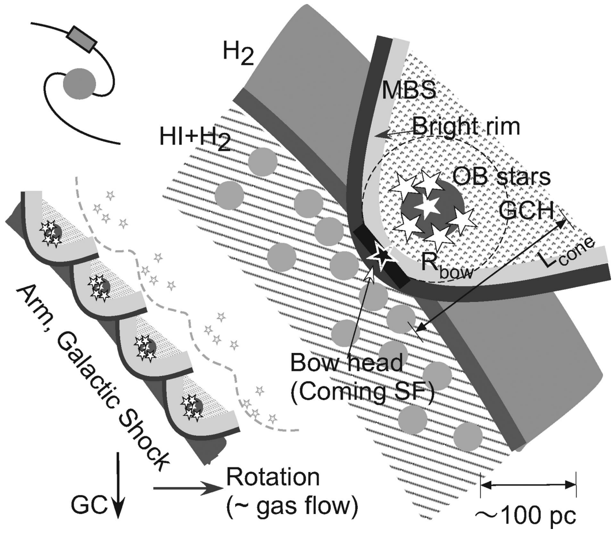

Fig. 2. Illustration of the molecular bow and GCH concave to the central OB star cluster proposed for the W 43 SF complex in the 4 kpc arm in the Galaxy (Sofue et al. 2018). The small insert shows an illustration for a wavy sequential star formation, discussed later.

We also show that MBSs are generally associated with giant cometary H II regions (GCH) on their down-stream sides, which may alternatively be called giant H II cone (GHC). Therefore, an MBS and a GCH make one single set of objects. So, they may be often referred to as either MBS or GCH.

The morphology and energetics (luminosity) of individual H II regions and OB clusters have been studied by optical imaging of M 83 using the Hubble Space Telescope (HST) (Chandar et al. 2010, 2014; Liu et al. 2013; Blair et al. 2014; Whitmore et al. 2011). High-resolution molecular gas distribution in M 83 has been extensively observed in the CO line emissions, and detailed comparative studies on H II regions are obtained using Atacama Large Millimeter/submillimeter Array (ALMA) high-resolution maps (Egusa et al. 2018; Hirota et al. 2018).

The structural relation between H II regions and molecular clouds has been one of the major subjects of star formation mechanics in the Galaxy, such as cloud–cloud collisions (McKee & Ostriker 2007). However, spatially-resolved relations between individual H II regions and dark clouds in external galaxies seem not to have been studied yet. We here focus on individual H II regions and their morphological relation with their associated dark clouds in M 83. We will show that their morphology is similar to the cometary cone structure modeled for G30.5 in the Galaxy. In order to explain the morphology, we propose qualitative models based on theories of bow shocks and expanded H II regions.

2 Extragalactic giant cometary H II regions (GCH) and molecular bow shocks (MBS)

We examine optical images taken from the STScI and NASA web sites of M 83 in λ438, 502, and 657 nm bands, observed with HST. We adopt the nucleus position at RA $= 13^{\mathrm{h}}37^{\mathrm{m}}00\overset{\mathrm{s}}{.}8$ and Dec $= -29^{\circ}51'56\overset{''}{.}0$ (Sofue & Wakamatsu 1994) and a distance of 4.5 Mpc (Thim et al. 2003). Figure 3 shows an HST image of M 83 at 657 nm, where GCHs associated with dark bow-shaped features (MBSs) are marked by white arcs. Figure 4 shows the same, but as a supplement for the outer region.

The identification of MBS+GCH was obtained by eye-identification as follows (numerical identification might be desirable, but is far beyond the scope of the present skills in imaging astronomy). First, it was easy to find H II regions and open clusters using each of the three color photographs (e.g., red for H II regions and blue for OB clusters), as well as assisted by the color-coded image as inserted in figure 3. Then, a search for associated dark lanes and clouds was obtained, and young, therefore bright, SF/H II regions are almost always associated with dark clouds. We excluded too faint or diffuse H II regions, which are either associated with diffuse clouds or not associated with dark clouds.

By pairing an H II region and a dark cloud, their morphological relation was looked into in detail individually. In most cases, an H II region is surrounded by an arc of dark lane in such a way that the H II region is lopsided and open to the interarm direction, while the other, brigher side is facing a concave bow-shaped dark lane, as illustrated in figure 2. Thus a discovered lopsided H II region and a molecular arc are here identified as a GCH and an MBS, assuming that a dark cloud is a molecular cloud.

The GCH and MBS are generally located on the down-stream sides of dark lanes of spiral arms. Each GCH is sheathed inside an MBS, and the inner wall of an MBS coincides with the outer front of the H II region composing a bright rim of Hα emission. Figure 2 illustrates the GCH/MBS structure.

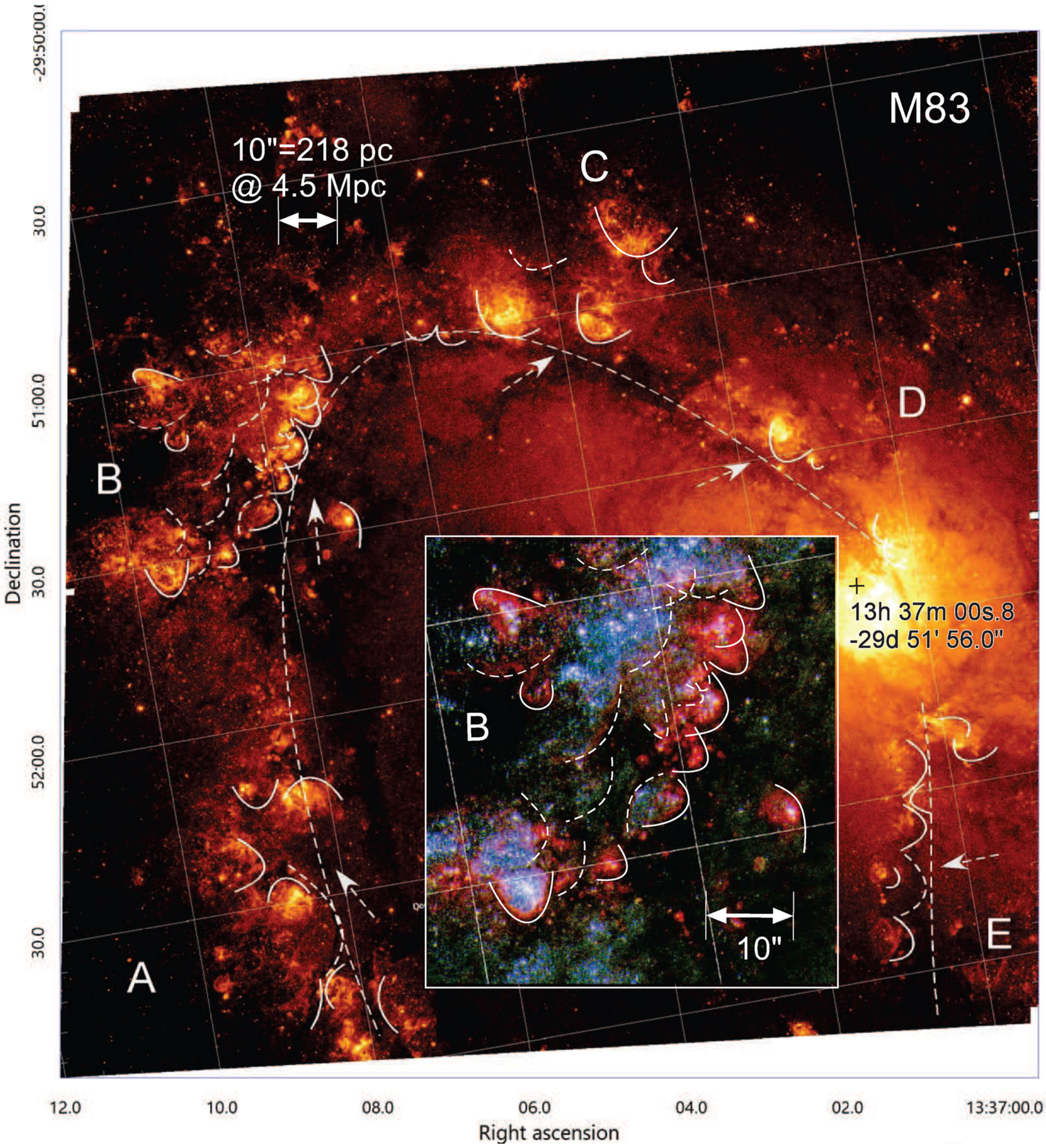

Fig. 3. Giant cometary H II regions (GCH) and molecular (dark) bow shocks (MBS) in M 83 marked by white arcs on a λ657 nm band image made from FITS formated image data base of the HST at STScI.[1] Spiral arm and rotation directions are indicated by a dashed line and arrows, respectively. The insert shows an enlargement of region B in RGB (657, 502, and 438 nm) color composite. The scale represents 10′ = 218 kpc at the distance of 4.5 Mpc. (Color online)

H II regions in M 83 have been classified into several categories according to their sizes and luminosities (Whitmore et al. 2011). We here classify H II regions in M 83 into three morphological types, summarized in table 1, and focus on Type III.

- Type I: H II bubbles around low-luminosity OB clusters with sizes smaller than the disk thickness and galactic shock thickness with full extent less than ∼30 pc. H II regions of categories 1–3 by Whitmore et al. (2011) are of this type.
- Type II: Bipolar cylindrical H II region open to the halo with a length comparable to the disk scale height. The wall looks like a hole in the disk with a diameter comparable to the disk thickness. Categories 3 and 4 are of this type.
- Type III: GCHs , alternatively GHCs, open to the halo as well as to inter-arm, which develop around luminous OB associations. The extent is comparable to or greater than the disk thickness and the width of galactic shock wave, with full extent as large as ∼100–200 pc. This type of H II region corresponds to categories 4–6. The GCH is characterized by the curvature $R_{\rm bow} \sim R_0$ of the bow/cometary

---

[1] ⟨http://www.stsci.edu/hst/wfc3/phot-zp-lbn⟩.

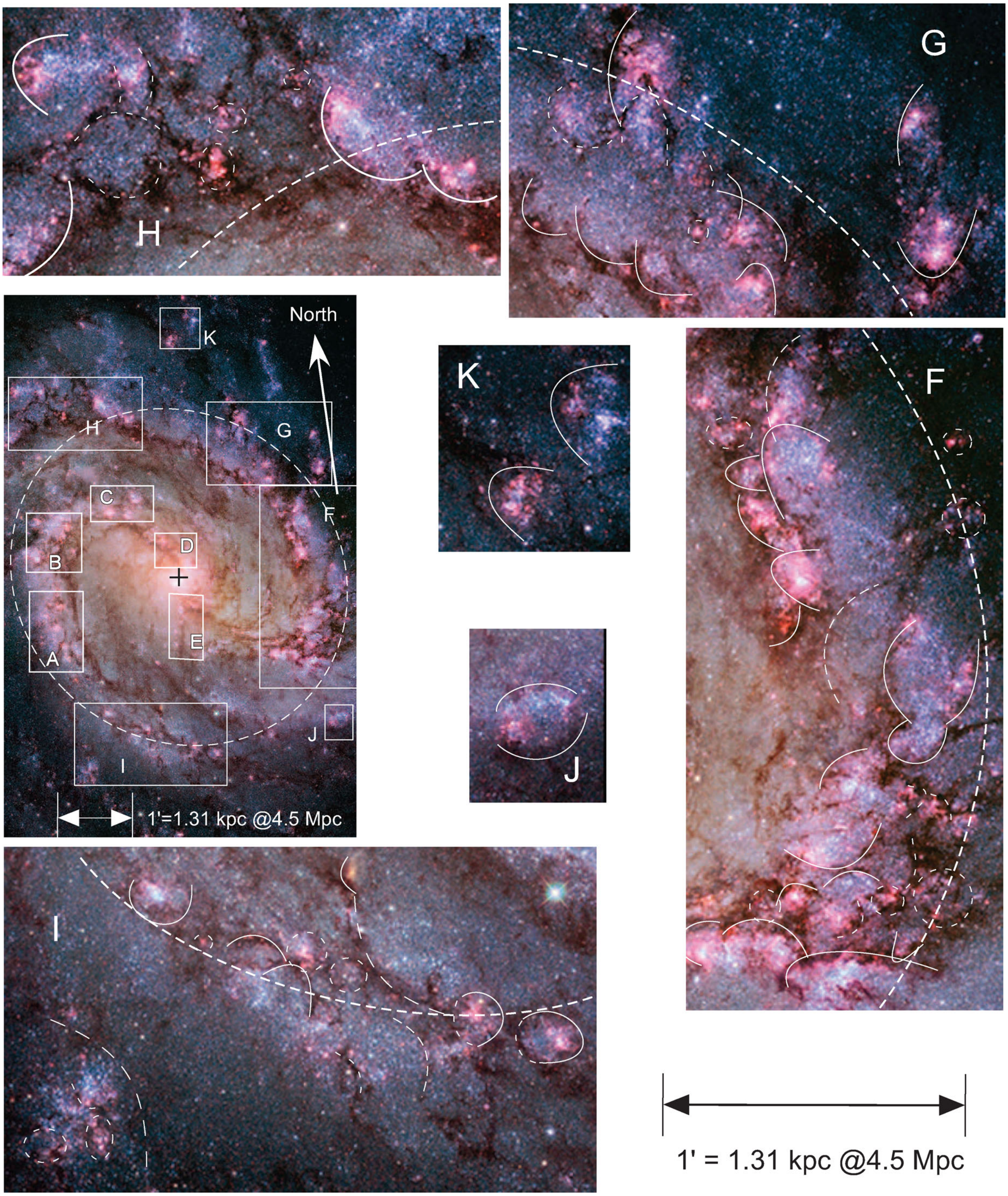

Fig. 4. Same as figure 3, but for outer regions of M 83. The large dashed ellipse and long-dashed lines indicate the corotation circle (Hirota et al. 2014). Thin dashed arcs and small ellipses are less clear or irregular MBS+GCH. The scale represents 1′ = 1.31 kpc at the distance of 4.5 Mpc. The color photo was taken from the web page of NASA [Image Credit: NASA, ESA, Hubble Heritage Team (STScI/AURA). Courtesy: Dr. W. P. Blair].[2] (Color online)

head, the axis length $L_{\rm cone}$, and the opening angle of the cone.

Using figure 3, where the coordinates are indicated, we measured the positions, bow-head curvatures $R_{\rm bow}$, and position angles (PA) of the GCH/MBS by fitting the arcs with a parabola. The measured values are listed in table 2.

Figure 5 shows the frequency distributions of $R_{\rm bow}$, estimated $L_{\rm UV}$, and offset of PA (δPV) from the vertical direction to the local spiral arm (dashed line in figure 3). In the statistics, we removed the GCH/MBS with $R_{\rm bow} > 150\,$pc,

---

[2] ⟨https://apod.nasa.gov/apod/ap140128.html⟩.

Table 1. Morphological classification of H II regions.

Type	Property	$R_{\rm bow}$ (pc)	$L_{\rm cone}$ (pc)	$L_{\rm UV}$ ($L_\odot$)
I	H II bubble	∼10	∼20	~ 10–10^2
II	Bipolar H II cylinder	∼20	∼20–50	$\sim 10^2$
III	Giant cometary H II cone	∼20–150	∼50–200	$\sim 10^2$–10^5

Table 2. Bow head position (offset from nucleus), $R_{\rm bow}$, PA of cone axis, and $L_{\rm UV}$.

	δRA (″)	δDec (″)	R_0 (pc)	PA (°)	$L_{\rm UV}$ ($L_\odot$)
A	147.7	− 54.0	160.4	− 60.1	0.47E+05
	139.7	− 47.3	71.3	45.2	0.41E+04
	137.7	− 51.0	177.1	82.8	0.63E+05
	143.5	− 38.4	169.6	67.6	0.55E+05
	135.9	− 29.8	46.8	0.0	0.12E+04
	133.5	− 26.6	52.5	72.7	0.16E+04
	133.3	− 17.4	47.2	− 5.5	0.12E+04
	143.1	− 13.3	83.9	− 0.8	0.67E+04
B	126.4	20.7	39.4	3.5	0.69E+03
	134.2	24.6	91.6	54.9	0.87E+04
	140.0	24.4	34.9	43.4	0.48E+03
	149.9	31.1	31.4	73.1	0.35E+03
	164.9	28.2	61.2	− 72.9	0.26E+04
	152.7	35.0	27.4	43.7	0.23E+03
	157.0	40.5	39.0	61.2	0.67E+03
	159.6	44.9	25.9	32.2	0.20E+03
	160.7	48.8	35.5	52.8	0.50E+03
	163.8	52.0	23.8	38.3	0.15E+03
	131.7	44.5	25.5	− 21.0	0.19E+03
	126.6	59.5	16.6	43.6	0.51E+02
	131.3	30.6	51.4	71.5	0.15E+04
	139.2	32.9	104.4	48.2	0.13E+05
	142.1	34.4	79.2	33.2	0.56E+04
	141.0	40.4	142.5	55.2	0.33E+05
	148.4	38.7	15.6	22.7	0.43E+02
	153.7	42.1	20.4	52.2	0.95E+02
	155.0	44.2	19.6	51.9	0.85E+02
	149.8	48.7	134.2	45.2	0.27E+05
	153.9	54.3	83.5	48.6	0.66E+04
	156.6	54.1	191.0	24.2	0.78E+05
	144.0	58.5	118.6	− 5.3	0.19E+05
C	70.2	55.4	37.7	− 4.4	0.61E+03
	73.7	53.9	28.0	− 37.1	0.25E+03
	82.7	54.1	84.7	− 31.6	0.68E+04
	98.1	50.5	54.2	− 34.0	0.18E+04
	90.0	64.3	94.8	− 35.8	0.96E+04
	109.6	58.9	45.6	− 47.0	0.11E+04
	106.2	63.5	91.7	− 22.4	0.87E+04
D	20.9	25.8	37.1	− 40.5	0.57E+03
	26.8	23.5	17.3	− 47.1	0.58E+02
	34.7	9.8	19.9	− 43.3	0.88E+02
	36.3	5.8	33.4	− 46.1	0.42E+03
E	29.6	− 58.9	59.2	64.3	0.23E+04
	33.2	− 49.9	90.3	58.8	0.83E+04
	28.4	− 47.8	32.8	40.4	0.40E+03
	34.9	− 40.3	38.3	62.2	0.63E+03
	32.8	− 34.8	24.3	76.0	0.16E+03
	36.8	− 29.2	79.6	− 82.0	0.57E+04
	43.4	− 29.8	52.5	− 35.4	0.16E+04
	42.8	− 22.1	76.0	− 21.4	0.49E+04

Table 3. Representative GCH parameters.

Parameter	Value
UV luminosity	$L_{\rm UV} \sim 10^4\,L_\odot$
Neutral gas density	$n \sim 10^2\,{\rm H\,cm^{-3}}$
Temp. of neutral gas	$T_{\rm n} \sim 20\,{\rm K}$
Temp. of H II gas	$T_{\rm e} \sim 10^4\,{\rm K}$
Scaling H II radius	$R_0 \sim 96.1\,{\rm pc}$
Cone-head radius	$r_0/R_0 = 0.5, 0.75, 1$
Shock scale length	$x_0/R_0 = 1$
Disk scale height	$z_0/R_0 = 1$
Background density in disk	$\epsilon_1 = 0.1$
—in halo	$\epsilon_2 = 0.01$

which are mostly weak dark lanes without luminous Hα nebulae (dashed arcs in figure 3).

The PA offset is concentrated around $\delta PA \sim 0^\circ$, indicating that the bows (cone) develop perpendicularly to the arms toward the outer inter-arm region. The cones are open toward the down-stream side of the gas flow in galactic rotation through the spiral density wave.

3 Qualitative models

3.1 Bow shock

In our recent paper (Sofue et al. 2018) we modeled the MBS G30.5 by applying Wilkin's (1996) analytical model for stellar-wind bow shock (figure 1). The distance Q of a bow front from the wind source is related to the elevation angle ϕ through

$$Q(\phi) = R_{\rm bow}\,{\rm cosec}\,\phi\sqrt{3(1-\phi\cot\phi)}. \tag{1}$$

Here, $R_{\rm bow}$ is the stand-off radius, defined as the distance of the front on the galactic plane from the wind source, which is measured as the smallest curvature of the bow head facing the gas flow. It is related to the momentum injection rate

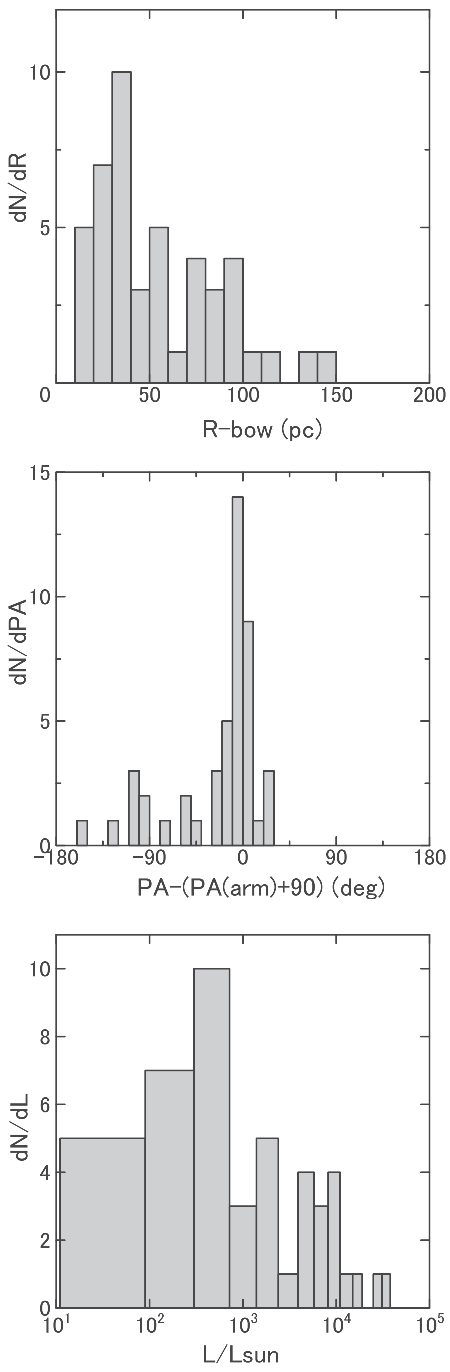

Fig. 5. Frequencies of R_{bow}, PA offset from the vector perpendicular to the local arm (dashed line in figure 3), and estimated L_{UV}.

$\dot{m}_{\mathrm{w}}$ by wind of velocity V_{w} from the central star and ram pressure by the in-flowing gas from outside by

$$R_{\mathrm{bow}} = \sqrt{\frac{\dot{m}_{\mathrm{w}} V_{\mathrm{w}}}{4\pi \rho V^2}}. \tag{2}$$

In the case of G30.5 we obtained $R_{\mathrm{bow}} \sim 54$ pc (Sofue et al. 2018), as shown in figure 1, where bow shapes calculated for $R_{\mathrm{bow}} = 25$, 50, and 75 pc are shown. Figure 6 shows the same calculated result compared with a GCH observed in region C of M 83.

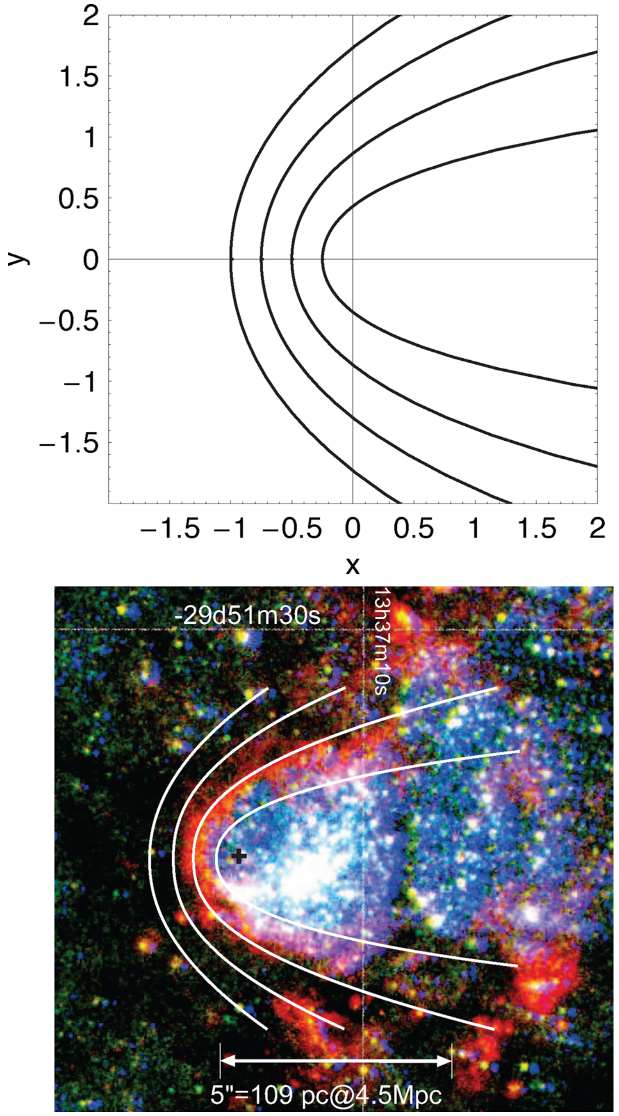

Fig. 6. Calculated bow shock front (top), and the same overlaid on a Type III GCH in M 83 from figure 3 on an arbitrary scale (bottom). The scale represents 5″ = 109 pc at the distance of 4.5 Mpc. (Color online)

3.2 H II cone

In order to model the front shape of an H II region in inhomogeneous ISM, we first consider the Strömgren radius in a uniform ISM given by

$$R_{\mathrm{H\,II}} \simeq \left(\frac{3 N_{\mathrm{UV}}}{4\pi n_{\mathrm{i}} n_{\mathrm{e}} \alpha_{\mathrm{r}}} \right)^{1/3}, \tag{3}$$

where N_{UV} is the UV photon number radiated by the OB stars, $\alpha_{\mathrm{r}} \sim 4 \times 10^{-13}\ \mathrm{cm}^{-3}\ \mathrm{s}^{-1}$ is the recombination rate, and n_{i} and n_{e} are the ion and electron densities, respectively.

We then assume that this equation holds in each small solid angle at any direction in which the density is assumed to be constant. We neglect the dynamical motion of gas inside the H II region. This approximation gives a qualitative shape to the front.

The ISM density variation is represented by an exponentially decreasing function in the x-direction perpendicular to the spiral arm with a scale width x_0. The z-directional (vertical) density profile is assumed to be represented by an inverse hyperbolic cosine function with a scale thickness z_0. Thus, the density in the galactic shock wave is expressed by

$$n = n_0 \left[\exp\left(-\frac{x}{x_0}\right) + \epsilon_1\right]\left[\cosh^{-1}\left(\frac{z}{z_0}\right) + \epsilon_2\right]. \tag{4}$$

Here, n_0 is a constant, and ϵ_1 and ϵ_2 are constants representing the relative background densities in the galactic plane and halo, respectively. The density increases exponentially at negative x, but decreases to the inter-arm value of ϵ_1 at $x \leq -2x_0$, beyond which the front cannot reach in the present cases.

The ion and electron densities are assumed to be related to the neutral gas density n through

$$n_\mathrm{e} \sim n_\mathrm{i} \sim n\frac{T_\mathrm{n}}{T_\mathrm{e}}, \tag{5}$$

where T_n and T_e are the temperatures of neutral and H II gas.

We now define the representative radius $R_{\mathrm{H\,II}}$ as the equilibrium radius of a spherical H II region in uniform gas with density n by

$$R_{\mathrm{H\,II}} \simeq \left[\frac{3N_\mathrm{UV}}{4\pi\alpha_\mathrm{r} n^2}\left(\frac{T_\mathrm{e}}{T_\mathrm{n}}\right)^2\right]^{1/3}. \tag{6}$$

Rewriting $N_\mathrm{UV} \sim L_\mathrm{UV}/h\nu$ with L and $h\nu$ being the luminosity of the central OB stars and UV photon energy over h912 A, respectively, we have

$$R_{\mathrm{H\,II}} \sim 96.1\left(\frac{L_\mathrm{UV}}{10^4}\right)^{1/3}\left(\frac{n}{10^2}\right)^{-2/3}\left(\frac{T_\mathrm{n}}{20}\right)^{-2/3}\left(\frac{T_\mathrm{e}}{10^4}\right)^{2/3}\ [\mathrm{pc}], \tag{7}$$

where L_UV is measured in $L_\odot$, n in $\mathrm{H\,cm^{-3}}$, and T_e in K. In table 3, we list the representative values of the parameters used in the model calculations.

Writing $R_{\mathrm{H\,II}} = \sqrt{x^2 + y^2 + z^2}$, we can express y as a function of x and z, which represents the front shape of a GCH, as

$$y = \sqrt{r_0^2\left(e^{-x/x_0} + \epsilon_1\right)^{-4/3}\left(\cosh^{-1} z/z_0 + \epsilon_2\right)^{-4/3} - x^2 - z^2}. \tag{8}$$

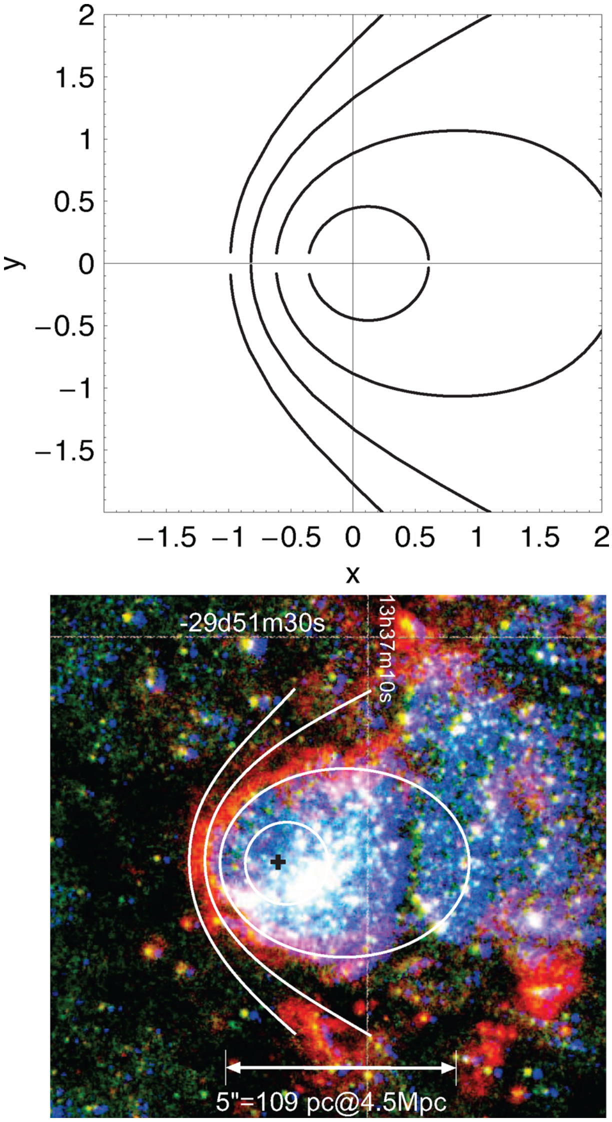

Fig. 7. Cometary front of an H II region for different central luminosities, and the same overlaid on a GCH in M 83 on an arbitrary scale. The scale represents 5″ = 109 pc at the distance of 4.5 Mpc. (Color online)

Here, r_0 is a parameter depending on the luminosity of the central OB association counted in terms of the head curvature of GCH R_0, which represents the radius for the neutral gas density $n = n_0$ at $(x, y, z) = (0, 0, 0)$. If we measure R_0, which is assumed to be equal to R_bow, we can estimate the UV luminosity L_UV of the exciting OB stars for a fixed gas density n_0.

In figure 7 we show calculated H II fronts for $r_0 = 0.5$, 0.75, and 1 in the (x, y) plane calculated for $\epsilon_1 = 0.1$. The scales are normalized by a scale length x_0. The bottom figure is an overlay of the calculated front on a GCH in M 83, where the scale is adjusted arbitrarily to fit the image.

In order to confirm that the qualitative model adopted here can reasonably reproduce a result by hydrodynamical simulation, we compare a calculated result of the H II front shape expanded in a sheet with density profile

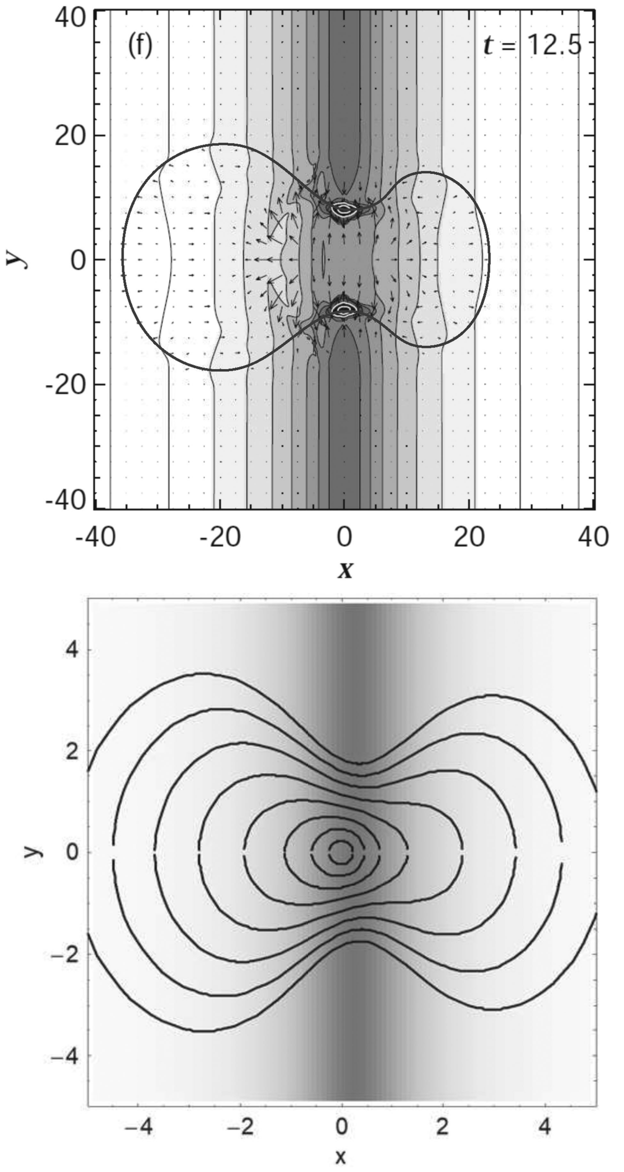

Fig. 8. Comparison of hydrodynamical simulation by Fukuda and Hanawa (2000) of an off-center expansion of the H II region (top) and front shape given by the present qualitative model (bottom) in a gas layer with density profile $\propto(1+x/x_0)^{-2}$.

$\propto(1+x/x_0)^2$ with a hydrodynamical simulation by Fukuda and Hanawa (2000). Figure 8 shows the comparison, and we may consider that the model is reasonable insofar as we are interested in the qualitative analysis of the front shapes.

Figure 9 shows 3D front shapes for $r_0 = 0.5, 0.7, 1$, and 1.5 for $x_0 = 1$, $z_0 = 1$, $\epsilon_1 = 0.1$, and $\epsilon_2 = 0.01$, where the scales are normalized by $R_{\rm H\,II}$. The front shapes vary according to the parameter $r_0 \propto R_0 \propto L^{1/3}\, n^{-2/3}$. For low-luminosity OB clusters, the H II front shows the spherical shape of a Type I. As the luminosity increases, the front is elongated in the z direction, resulting in a Type II bipolar cylinder open to the halo. As r_0 increases further, the shape becomes more open into the inter-arm region and to the halo, resulting in a Type III for GCH.

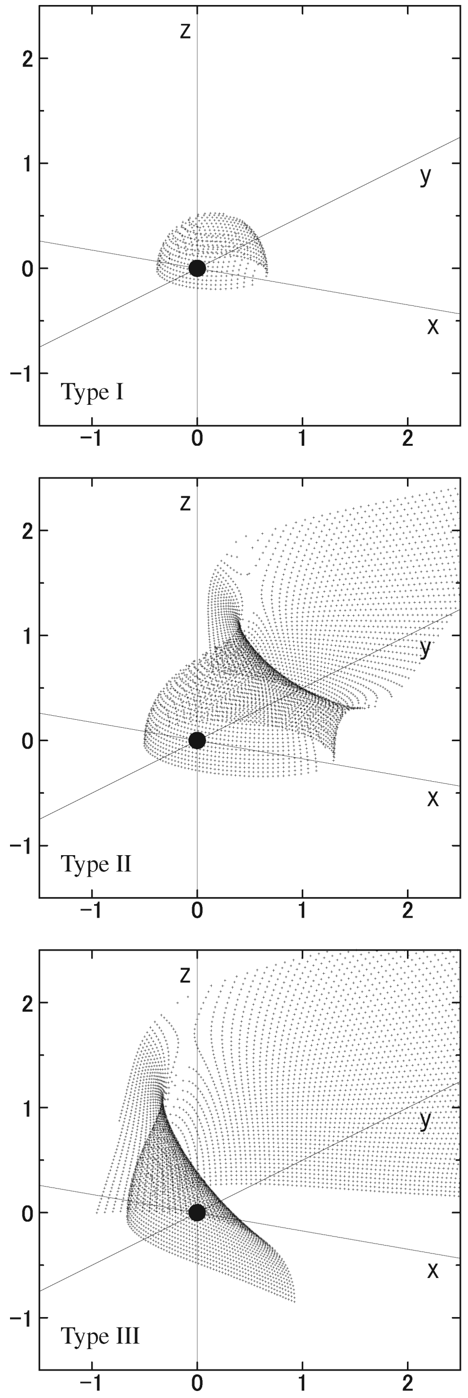

Fig. 9. H II region shapes of Types I (bubble), II (cylinder), and III (GCH cone) according to $r_0 = 0.5$, 0.7, and 1 for fixed parameters of $x_0 = 1$, $z_0 = 1$, $\epsilon_1 = 0.1$, and $\epsilon_2 = 0.01$.

3.3 UV luminosity

The ^{12}CO($J = 1$–0) integrated intensity toward dark lanes in M 83 has been observed to be $I_{\rm CO} \sim 150$ K km s^{-1} (Egusa et al. 2018), which yields a molecular gas density of $n \sim 200\,{\rm H\,cm^{-3}}$ for an assumed disk thickness of ∼50 pc and a conversion factor of $2 \times 10^{20}{\rm H\,cm^{-2}}$ (K km s^{-1})$^{-1}$ (Bolatto et al. 2013). Given the gas density, UV luminosities $L_{\rm UV}$ of exciting OB stars are estimated for the measured $R_0 \sim R_{\rm bow}$ using equation (7) as $L_{\rm UV} \sim 4 \times 10^2 (R_0/96.1)^3\, L_\odot$. Thus estimated luminosities $L_{\rm UV}$ range from $\sim 10^3$ to $\sim 10^5\, L_\odot$ (table 2), and may be compared with the visual luminosities of $L_{\rm v} \sim \times 10^4$–$10^6\, L_\odot$ (absolute visual magnitudes $M_{\rm v} \sim -6$ to -10) of OB clusters in M 83 (Chandar et al. 2010).

3.4 GCH sheathed inside MBS

The MBS is composed of low-temperature and high-density molecular gas. On the other hand, the GCH is high-temperature and low-density H II gas expanded around OB clusters. However, both the MBS and GCH show a similar morphology (figures 6 and 7), and occur simultaneously. An H II region encountering a supersonic gas flow in galactic rotation makes a bow shock on its up-stream side, and is blown off toward the down-stream, making an open cone shape.

The interaction of MBS and GCH may cause mutual deformation. The expansion of GCH is suppressed by the MBS on the up-stream side, while it becomes more free in the tail. The side wall of MBS also suppresses the H II expansion, and guides the H II gas into a more collimated cone.

3.5 Dual-side compression and wavy sequential star formation

The GCH and MBS act as a mutually triggering mechanism of star formation in such a way that GCH compresses the stacked molecular gas at the bow head from the inside, and MBS compresses molecular clouds from the outside. The supersonic flow from the spiral arm's gravitational potential conveys and supplies molecular clouds to the bow head.

Thus, the bow head becomes an efficient SF site as a result of the "dual dynamical compression" sandwiched between the MBS and the GCH. This enhances galactic-scale compression of molecular clouds along the galactic shock, and makes the star formation rate one order of magnitude higher than that by cloud–cloud collisions (e.g., McKee & Ostriker 2007).

MBS and GCH appear in a chain along the arms (figures 3 and 4), and form a wavy array of SF regions along the galactic shock wave. Furthermore, the bow waves from the MBS encounters the neighboring waves, triggering star formation in dense regions between MBSs in a sequential way (figure 2).

3.6 High SF rate

It has been argued that the cloud–cloud collision is an efficient mechanism of star formation (McKee & Ostriker 2007), and the star formation rate (SFR) is given by $1/t_{\rm col}$, where $t_{\rm col}$ is the cloud–cloud collision time given by

$$t_{\rm col} \sim \frac{\rho_{\rm cloud} R_{\rm cloud}}{\rho_{\rm mean} \sigma} \sim 10^7\ {\rm yr}. \tag{9}$$

Here, $\rho_{\rm cloud} \sim 10^3\,{\rm H\,cm^{-3}}$ is GMC's gas density, $\rho_{\rm mean} \sim 200\,{\rm H\,cm^{-3}}$ is the averaged density of molecular gas, $R_{\rm cloud} \sim 30$ pc is the mean cloud radius, and $\sigma \sim 7\,{\rm km\,s^{-1}}$ is the ISM turbulent velocity. On the other hand, the cloud–bow head collision time $t_{\rm bow}$ is given by

$$t_{\rm bow} \sim \frac{\rho_{\rm cloud} R_{\rm cloud}}{\rho_{\rm mean} (V_{\rm rot} - V_{\rm p}) \sin\ p} \sim 10^6\ {\rm yr}, \tag{10}$$

where $V_{\rm rot} \sim 200\,{\rm km\,s^{-1}}$ is the rotation velocity of the galaxy, $V_{\rm p} \sim R\Omega_{\rm p}$ (with $R \sim 2$ kpc and $\Omega_{\rm p} \sim 20\,{\rm km\,s^{-1}\,kpc^{-1}}$) is the pattern velocity, and $p \sim 30°$–$80°$ is the pitch angle of the spiral arm or the gaseous bar in M 83.

We may therefore conclude that the SF rate $1/t_{\rm bow} \sim 10^{-6}\,{\rm yr^{-1}}$ due to the galactic shock wave assisted by the MBS+GCH dual compression is an order of magnitude higher than the SF rate $1/t_{\rm col} \sim 10^{-7}\,{\rm yr^{-1}}$ due to cloud–cloud collisions.

3.7 Cometary vs. cylindrical types

Our model calculation showed that the cometary structure is more efficiently produced when the density gradient is sharper toward the down-stream side of the arm and the flow velocity against the bow head is faster. Such conditions may be present in grand-designed arms and bars with the galactic rotation that is significantly faster than the pattern speed. In fact, cometary H II regions are generally observed in two-armed interacting spiral galaxies like M 51 or in barred spirals like M 83 and NGC 1300.

On the other hand, H II regions in flocculent arms such as M 33 and NGC 2403 tend to show a cylindrical or spherical morphology. This could be explained by the arms co-rotating with the galactic rotation, such that an H II region expands more symmetrically in the arm's center. Similarly, in distant arms in corotation with the galactic rotation, H II regions also tend to have a spherical or cylindrical morphology. These facts may be used to measure the corotation radius by observing the directions of the H II cones with respect to the arms.

In order to check this idea, we have traced round, or irregular, MBSs and GCHs in the regions outside the corotation in regions G to K in figure 4, where the big ellipse and long-dashed lines indicate a corotation circle of radius 140″ at position angle 225° and inclination 24° (Hirota et al. 2014). Although the tracing was rather inaccurate because of the lack of bright and clear-edged H II regions, we found a number of irregular cometary H II regions and less clear MBSs, as indicated by dashed arcs and small ellipses. The fraction of irregular cases is larger than in the inner arms as can be seen in figure 3. This may imply that the corotation indeed takes place near the indicated corotation circle.

4 Summary

Using optical images of nearby spiral galaxies taken with the HST (NASA APOD), we identified many sets of GCHs and MBSs in the barred spiral galaxy M 83. We classified H II regions into Types I–III according to their degree of openness into the halo and disk. We argued that the GCHs and MBSs are general phenomena in galactic shock waves.

The cone-shaped morphology of GCHs is qualitatively explained by a model of an evolved H II sphere expanded in inhomogeneous ISM with a steep density gradient, and the MBS is understood by the bow shock theory. Since in the actual galactic condition the GCH and MBS are coupled with each other, the dual side compression of gas at the MBS/GCH heads makes the SFR more efficient than the SFR by cloud–cloud collisions by a factor of 10.

We have further examined high-resolution images of other galaxies from HST and the Subaru Telescope, and found that GCHs and MBSs are general phenomena in grand-designed spiral arms and/or bars. A full atlas of GCHs/MBSs in nearby galaxies will be presented in a separate paper.

Acknowledgments

The optical images of M 83 were reproduced from the web sites of STSci at ⟨http://www.stsci.edu/hst/wfc3/⟩ and NASA at ⟨https://apod.nasa.gov/apod/⟩.

References

Arce, H. G., & Goodman, A. A. 2002, ApJ, 575, 928
Arthur, S. J., & Hoare, M. G. 2006, ApJS, 165, 283
Blair, W. P., et al. 2014, ApJ, 788, 55
Bolatto, A. D., Wolfire, M., & Leroy, A. K. 2013, ARA&A, 51, 207
Campbell-White, J., Froebrich, D., & Kume, A. 2018, MNRAS, 477, 5486
Chandar, R., et al. 2010, ApJ, 719, 966
Chandar, R., Whitmore, B. C., Calzetti, D., & O'Connell, R. 2014, ApJ, 787, 17
Deharveng, L., et al. 2015, A&A, 582, A1
Dyson, J. E. 1975, Ap&SS, 35, 299
Egusa, F., Hirota, A., Baba, J., & Muraoka, K. 2018, ApJ, 854, 90
Fukuda, N., & Hanawa, T. 2000, ApJ, 533, 911
Gómez, G. C., & Cox, D. P. 2004a, ApJ, 615, 744
Gómez, G. C., & Cox, D. P. 2004b, ApJ, 615, 758
Hirota, A., et al. 2014, PASJ, 66, 46
Hirota, A., et al. 2018, PASJ, 70, 73
Liu, G., et al. 2013, ApJ, 778, L41
McKee, C. F., & Ostriker, E. C. 2007, ARA&A, 45, 565
Martos, M. A., & Cox, D. P. 1998, ApJ, 509, 703
Ogura, K. 1995, Ap&SS, 224, 151
Reid, M. J., & Ho, P. T. P. 1985, ApJ, 288, L17
Reipurth, B., Heathcote, S., Morse, J., Hartigan, P., & Bally, J. 2002, AJ, 123, 362
Sofue, Y. 1985, PASJ, 37, 507
Sofue, Y., et al. 2018, PASJ, in press (doi: 10.1093/pasj/psy094)
Sofue, Y., & Wakamatsu, K. 1994, AJ, 107, 1018
Steggles, H. G., Hoare, M. G., & Pittard, J. M. 2017, MNRAS, 466, 4573
Thim, F., Tammann, G. A., Saha, A., Dolphin, A., Sandage, A., Tolstoy, E., & Labhardt, L. 2003, ApJ, 590, 256
van Buren, D., Mac Low, M.-M., Wood, D. O. S., & Churchwell, E. 1990, ApJ, 353, 570
Whitmore, B. C., et al. 2011, ApJ, 729, 78
Wilkin, F. P. 1996, ApJ, 459, L3